NANO LETTERS

pubs.acs.org/NanoLett

Letter

Two Birds with One Stone: Concurrent Ligand Removal and Carbon Encapsulation Decipher Thickness-Dependent Catalytic Activity

Kun Guo, Litao Chang, Ning Li, Lipiao Bao, Samir de Moraes Shubeita, Aliaksandr Baidak, Zhixin Yu,* and Xing Lu*

Cite This: *Nano Lett.* 2022, 22, 8763−8770

Read Online

ACCESS | Metrics & More | Article Recommendations | Supporting Information

ABSTRACT: A carbon shell encapsulating a transition metal-based core has emerged as an intriguing type of catalyst structure, but the effect of the shell thickness on the catalytic properties of the buried components is not well known. Here, we present a proof-of-concept study to reveal the thickness effect by carbonizing the isotropic and homogeneous oleylamine (OAm) ligands that cover colloidal MoS_2. A thermal treatment turns OAm into a uniform carbon shell, while the size of MoS_2 monolayers remains identical. When evaluated toward an acidic hydrogen evolution reaction, the calcined MoS_2 catalysts deliver a volcano-type activity trend that depends on the calcination temperature. Rutherford backscattering spectrometry and depth-profiling X-ray photoelectron spectroscopy consistently provide an accurate quantification of the carbon shell thickness. The same variation pattern of catalytic activity and carbon shell thickness, aided by kinetic studies, is then persuasively justified by the respective limitations of electron and proton conductivities on the two branches of the volcano curve.

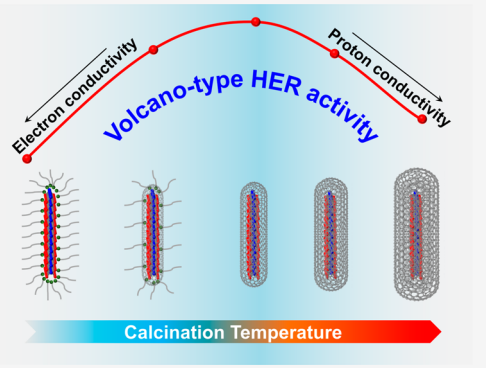

KEYWORDS: *encapsulation, shell thicknesses, molybdenum disulfide, electrocatalysts, hydrogen evolution reaction*

A pressing issue recognized by the catalysis community is that the applied solid catalysts often experience uncontrollable structural and compositional variations under harsh reaction conditions.[1−6] One solution that is being strongly pursued is to cover the catalysts with a carbon shell that protects the components beneath. These peculiar types of core−shell catalysts have demonstrated fascinating advantages, such as resistances to agglomeration, corrosion, and oxidation, reaction selectivity control, and an electron transfer effect.[7−9] However, the influence of the carbon shell structure on the buried core has been poorly elaborated due inevitably to the challenge of fine-tuning the shell structural factors while retaining identical inner cores.

One of the intriguing structural factors of a carbon shell is its thickness along the radial direction. A critical, yet often ignored, question is how the thickness of the carbon shell dictates the catalytic behavior, especially from the perspective of proton-coupled electron transfer that lays the foundation of many electrochemical reactions.[10,11] In the cases of single- and few-layer graphene, previous studies have verified that protons can penetrate through, allowing their accessibility to the core materials beneath.[12−16] However, a carbon shell that is too thick may block the reactants from accessing the active sites and detain the products from diffusing away. The shell thickness also affects the synergistic interactions between the metal core and the outer few carbon layers that are catalytically relevant. Theoretical calculations by Bao and co-workers revealed that the electron transfer between the carbon shell and metal core gradually intensifies and remains steady when the shell is thicker than three graphene layers.[17] Therefore, the effect of shell thickness deserves considerable attention to precisely evaluate the catalysts of interest, but relevant in-depth studies on this aspect are still lacking.

The key to deciphering the shell thickness effect is the controllable synthesis of carbon-encapsulated materials with well-defined structural parameters. Furnace pyrolysis is the prevailing route to yield metal-based cores embedded in carbon shells.[18−20] Nonetheless, it is extremely difficult to control the structures and compositions of both the core and shell because the process is largely empirical, making the precise discrimination of the catalytic contributions of core and shell difficult.[21−23] Colloidal synthesis in the presence of organic ligands has demonstrated its competence to tailor-make low-dimensional transition metal-based nanomaterials.[24−26] Calcination is often required to recover ligand-stripped catalysts, but what indeed occurs is that calcination does not remove all the ligands but turns part of them into carbon layers covering inner

Received: August 10, 2022
Revised: September 22, 2022
Published: September 26, 2022

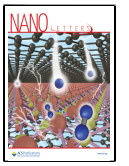

https://doi.org/10.1021/acs.nanolett.2c03181
Nano Lett. 2022, 22, 8763−8770

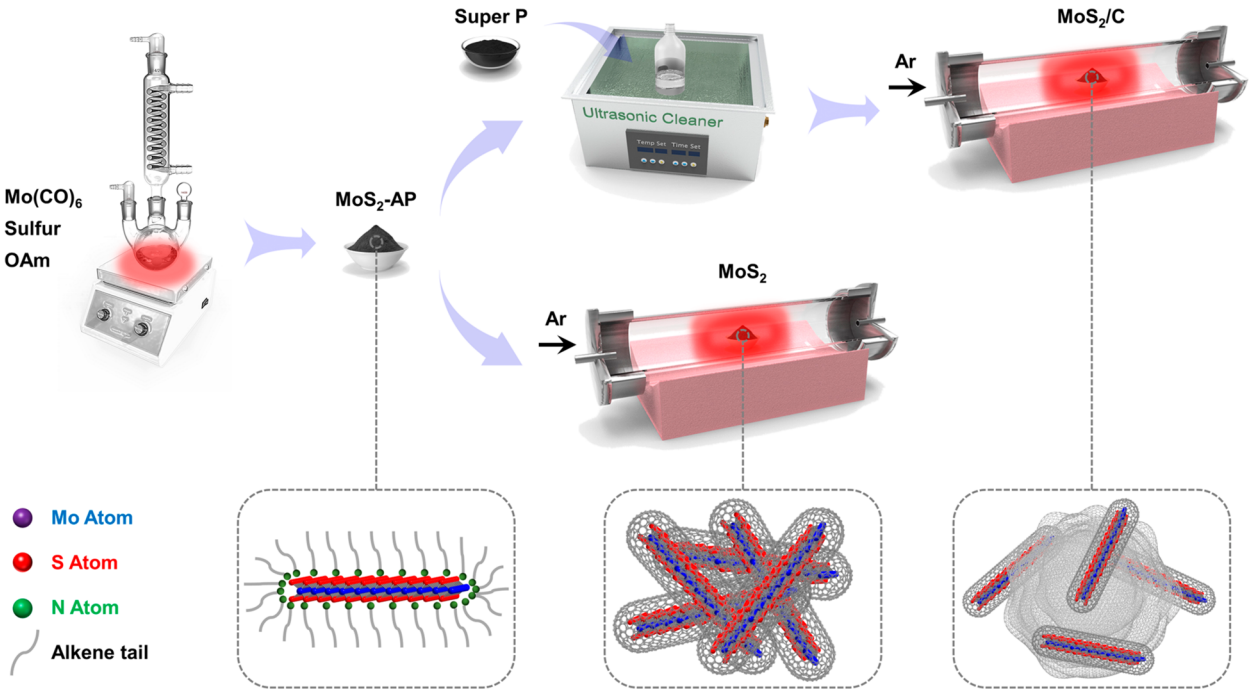

Figure 1. Schematic illustration of the colloidal synthesis of OAm-ligated MoS_2 monolayers and the postcalcination to produce MoS_2/C and MoS_2.

cores.[27−29] In light of the colloidal nanomaterials with narrow size distributions and homogeneous ligand coverage, calcination of ligand-capped nanomaterials holds the potential to solve two problems at one time. On one hand, the detrimental ligands that sterically and chemically block the metal active sites can be efficiently eliminated. On the other hand, the isotropic and homogeneous surface ligands can be converted into uniform carbon shells with a well-defined and adjustable thickness.[30] The resulting products thus serve as a desirable prototype to investigate the thickness effect of the carbon shell on the catalytic properties of encased cores.[31]

Drawing on the preceding synthesis of ligated MoS_2 monolayers,[32] we take one step further by calcining the monolayers at controlled temperatures in the range of 200−600 °C to carbonize the ligands without affecting the size of the MoS_2 core. The hydrogen evolution reaction (HER) activity in acids of the calcined products is found to be dependent on the calcination temperature, forming a volcano-type activity curve. Microscopic and spectroscopic characterizations unambiguously disclose the formation of a carbon shell around the MoS_2 monolayers. The relative thickness of the carbon shell is further quantified by Rutherford backscattering spectrometry and depth-profiling X-ray photoelectron spectroscopy. The results not only are closely in accord with each other but also decipher the volcano-type thickness-dependent activity, which is attributed to the tradeoff between electron conductivity (ligand coverage) and proton conductivity (mass transfer).

Figure 1 illustrates the colloidal synthesis and postcalcination treatments of unsupported MoS_2 and Super P carbon supported MoS_2 (MoS_2/C). Oleylamine (OAm) functions as both the solvent and the surfactant.[33−36] The applicability of ethanol/hexane washing for OAm removal is first tested. OAm-ligated Pd and Ni_2P nanoparticles are also prepared following similar procedures (Figure S1). Attenuated total reflection Fourier transform infrared (ATR-FTIR) spectra of the obtained materials and reference chemicals confirm the existence of OAm according to the absorption peaks arising from various vibrational modes in the OAm molecule (Figure S2). After solvent washing, OAm is significantly eliminated for Pd and Ni_2P but barely removed for MoS_2-AP, indicating the strong coordination between OAm and MoS_2.

A transmission electron microscope (TEM) image of MoS_2-AP is shown in Figure 2a. Randomly oriented dark lines are discerned, which stem from the side view of disordered MoS_2 monolayers. A statistical count and a corresponding Gaussian fit of at least 200 monolayers give an ultrafine lateral size of 4.3 ± 1.1 nm. The X-ray diffraction (XRD) patterns of MoS_2-AP and MoS_2/C-AP (Figure S3) confirm the hexagonal 2H-MoS_2 phase (JCPDS card no. 37-1492). The broad characteristic peaks at 32.7 and 58.3°, corresponding to the (100) and (110) in-plane diffraction, respectively, manifest the low crystallinity of MoS_2. The absence of the (002) characteristic peak at 14.3° in Figure S4 further demonstrates the monolayer structure, in stark contrast to the highly crystalline commercial MoS_2 (c-MoS_2). The (004) peak originally located at 29.0° of standard 2H-MoS_2 is shifted to 18.5°, indicating an extended interplanar spacing along the *c* axis according to Bragg's law.

To remove the ligands, we calcined the MoS_2-AP and MoS_2/C-AP at 200−600 °C. Analogous dark lines in MoS_2-400 (Figure 2b) are observed with an almost identical lateral size. Moreover, the monolayers are attached to an amorphous carbon substrate resulting from OAm carbonization (*vide infra*). In comparison, MoS_2/C is also annealed at 400 °C (Figure 2c). The spherical carbon particles of Super P with clear lattice fringes are discerned alongside the dark lines of MoS_2. Again, the average lateral size of MoS_2 monolayers barely vary from those of MoS_2-AP and MoS_2-400. XRD patterns in Figure 2d indeed show that the structure and size of MoS_2 are well retained at calcination temperatures of even up to 600 °C. Super P itself is very stable during sintering (Figure S5). This result is hence linked to the carbon shell that affords high sintering resistance and structural stability. Scanning electron microscopy unveils the consistent surface morphology of Super P and the calcined MoS_2/C (Figure S6), distinct from that of the calcined MoS_2 (Figure S7).

https://doi.org/10.1021/acs.nanolett.2c03181
Nano Lett. 2022, 22, 8763−8770

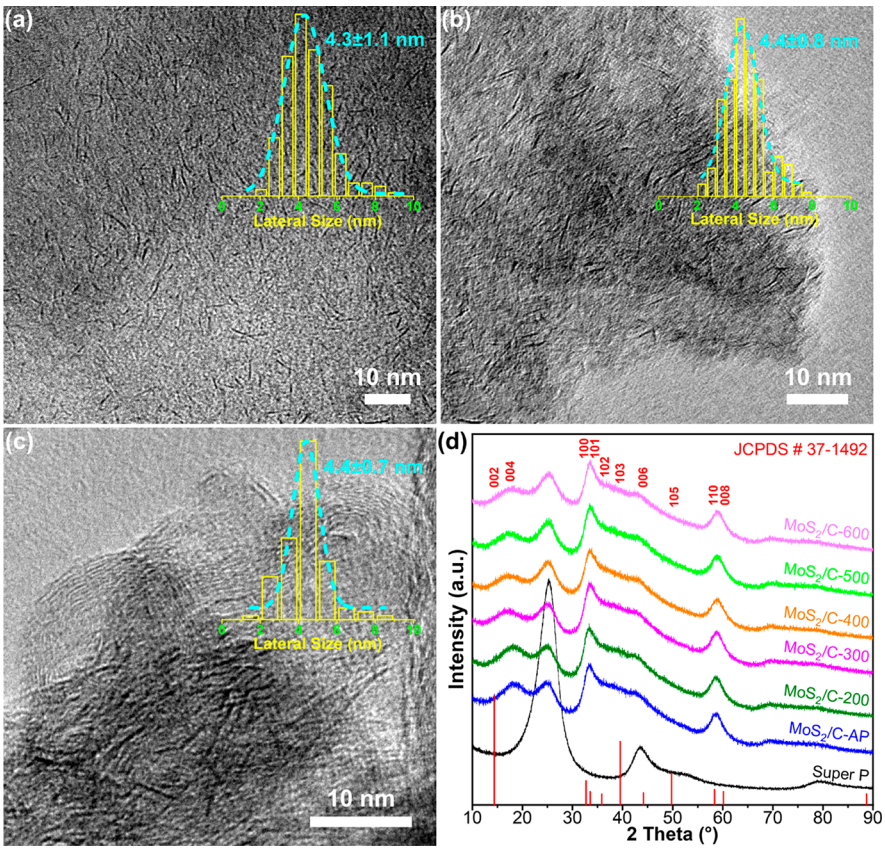

Figure 2. TEM images and the corresponding lateral size distributions of MoS_2-AP (a), MoS_2-400 (b), and MoS_2/C-400 (c). (d) XRD patterns of the calcined MoS_2/C, MoS_2/C-AP, and Super P.

Figure 3a shows the ATR-FTIR spectra of calcined and as-prepared MoS_2/C. The prominent absorption peaks from the most representative aliphatic tail of OAm, enlarged in the right panel, hardly appear at 400 °C and above, manifesting the complete transformation of OAm. To preclude the effect of Super P carbon, we also compare the ATR-FTIR spectra of MoS_2-AP and calcined MoS_2 (Figure 3b). It is again found that a threshold of 400 °C is necessary for the total elimination of OAm ligands. The Raman spectra of supported MoS_2 in Figure 3c present two major peaks at 1350 and 1599 cm^{-1}, ascribed to the D and G bands of graphitic structures, respectively. The Raman spectra of the unsupported MoS_2 are displayed in Figure 3d. For both MoS_2-200 and MoS_2-AP, D and G bands are not observed. When the temperature is elevated to 300 °C, both D and G bands appear, directly evidencing the carbon formation.[37] The higher graphitization degree of the resultant carbon calcined at a higher temperature is reflected in the increasing I_D/I_G ratios. Moreover, two minor peaks located at lower Raman shifts, corresponding to the E^1_{2g} and A_{1g} vibrational modes of lamellar MoS_2 (Figure S8), are discerned. Compared to c-MoS_2, both E^1_{2g} and A_{1g} bands are shifted for all the supported and unsupported samples, especially those annealed at relatively high temperatures. The red shift of the A_{1g} band is anticipated due to the monolayer structure.[38,39] However, the E^1_{2g} band is not blue-shifted, which is interpreted as being a disturbance of the defective layer structure and ultrafine lateral size of MoS_2.[40−42]

A depth-profiling X-ray photoelectron spectroscopy (XPS) analysis coupled with 300 eV Ar^+ etching is further performed to probe the elemental composition and speciation at different depths. Commercial c-MoS_2 is included as a reference (Figure S9). All of the full survey XPS spectra of the calcined MoS_2 at three etching stages identify the elements C, N, O, S, and Mo (Figure S10). The inconspicuous C 1s peak changes of each sample before and after etching can be ascribed to the random orientation of MoS_2 monolayers throughout the carbon shell (Figure S11). In contrast, Figure S12 shows that the C 1s peak is the smallest for MoS_2-400 among the calcined MoS_2 etched for 90 s. The N 1s region is close to that of Mo 3p, and the XPS spectra are then deconvoluted into Mo^{4+} $3p_{3/2}$, Mo^{6+} $3p_{3/2}$, and N 1s (Figure S13). The N 1s peak shrinks with an increase in the calcination temperature and disappears at 400 °C, verifying the complete removal of OAm. The Mo 3d and S 2p XPS spectra after 90 s of etching are shown in Figure 3e,f, respectively. As the calcination temperature increases, all of the doublet peaks of Mo 3d move to lower binding energies, indicating that fewer 3d electrons are transferred from MoS_2 to OAm as OAm is being gradually removed. After OAm removal, the Mo^{4+} $3d_{5/2}$ and $3d_{3/2}$ peaks are positioned at almost the same binding energy as that of c-MoS_2 (Figure S14). In Figure 3f, the S $2p_{3/2}$ and $2p_{1/2}$ doublets are shifted to higher binding energy, implying that fewer electrons are withdrawn from S atoms as OAm ligands are eliminated. This is in contradiction with the fact that more 3d electrons are available by Mo as fewer are transferred to N. It is inferred that N−H···S hydrogen bonds could be formed to allow electron withdrawal from adjacent H atoms to low-valent S atoms. Removal of OAm thus results in the upward shifting of the binding energy of S 2p electrons to the same positions as in c-MoS_2 (Figure S14).

https://doi.org/10.1021/acs.nanolett.2c03181
Nano Lett. 2022, 22, 8763−8770

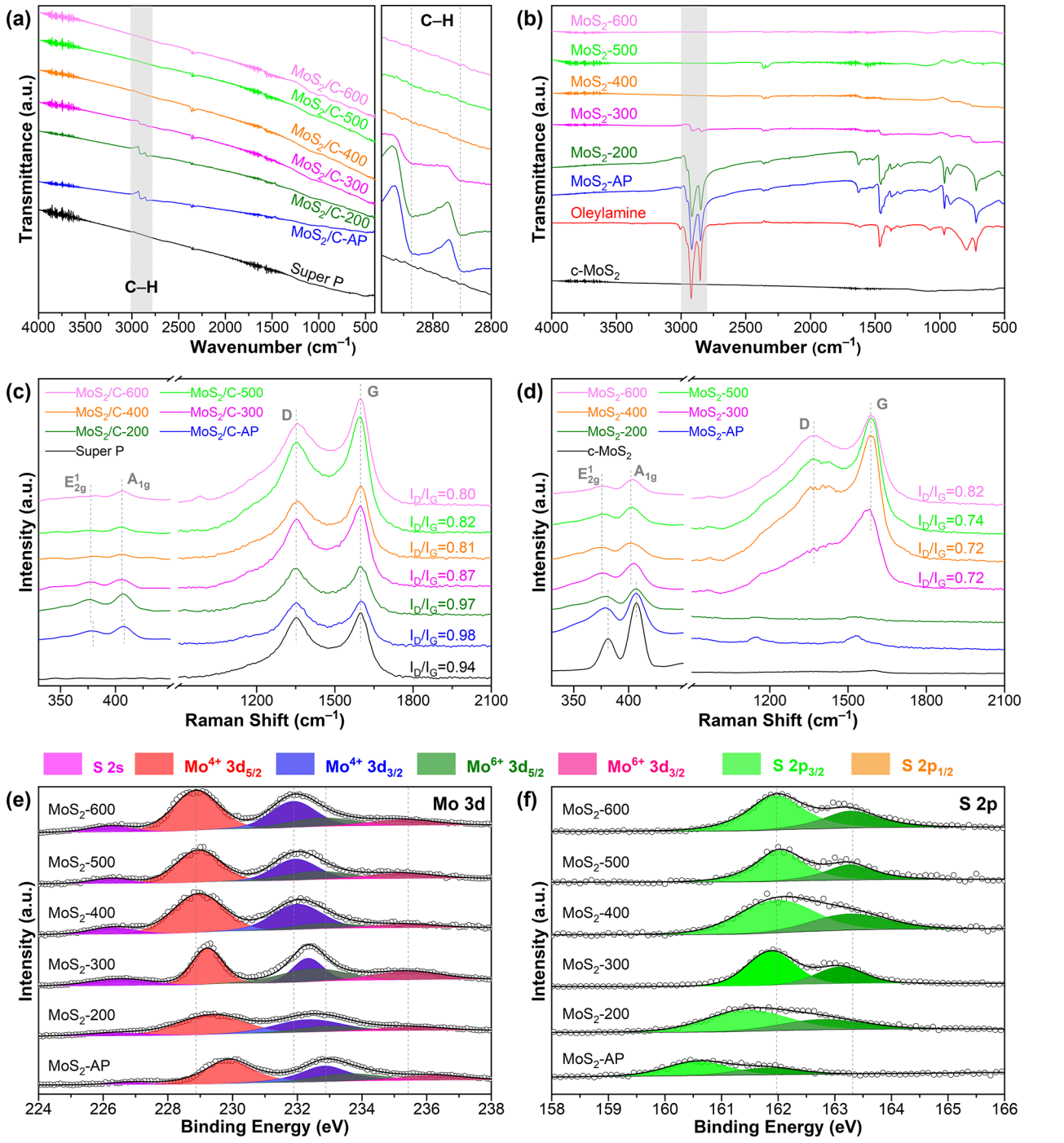

Figure 3. ATR-FTIR and Raman spectra of (a, c) the calcined, as-prepared MoS_2/C and Super P, and (b, d) the calcined, as-prepared MoS_2 and c-MoS_2. The right panel of (a) is an enlargement of the highlighted region that represents the C−H bond stretching vibration. The corresponding I_D/I_G ratios are indicated in (c, d). High-resolution XPS spectra of Mo 3d (e) and S 2p (f) regions of the calcined and the as-prepared MoS_2.

The HER activity of the calcined MoS_2/C is assessed in Ar-saturated 0.5 M H_2SO_4. Figure 4a shows the *iR*-compensated linear sweep voltammetry (LSV) polarization curves of the catalysts being studied. The overpotential at a current density of 10 mA cm^{-2} (η_{10}) is compared in the upward axis of the radar chart in Figure 4b. Despite the ultrafine lateral size of MoS_2/C-AP, its η_{10} value is found to be close to that of c-MoS_2/C, indicating the poor HER activity of MoS_2/C-AP. Calcination of MoS_2/C-AP at 200 and 300 °C leads to a gradually reduced η_{10} value and improved activity. When the calcination reaches 400 °C, η_{10} is reduced by 280 and 130 mV compared to the values for Super P and MoS_2/C-AP, respectively. However, at even higher temperatures, η_{10} starts to increase for MoS_2/C-500 and MoS_2/C-600, indicating their deteriorated HER activities. Figure 4c shows the Tafel plots, and the derived Tafel slopes are presented in the rightward axis of Figure 4b. MoS_2/C-400 delivers the smallest Tafel slope of 76 mV dec^{-1}. The other catalysts annealed at lower or higher temperatures have values larger than 118 mV dec^{-1}. As elaborated in Note S1, the rate-determining step (RDS) for c-MoS_2/C should be the Volmer step that involves electron transfer and proton adsorption at the active sites (H*), in agreement with the facts that hydrogen adsorption

https://doi.org/10.1021/acs.nanolett.2c03181
Nano Lett. 2022, 22, 8763−8770

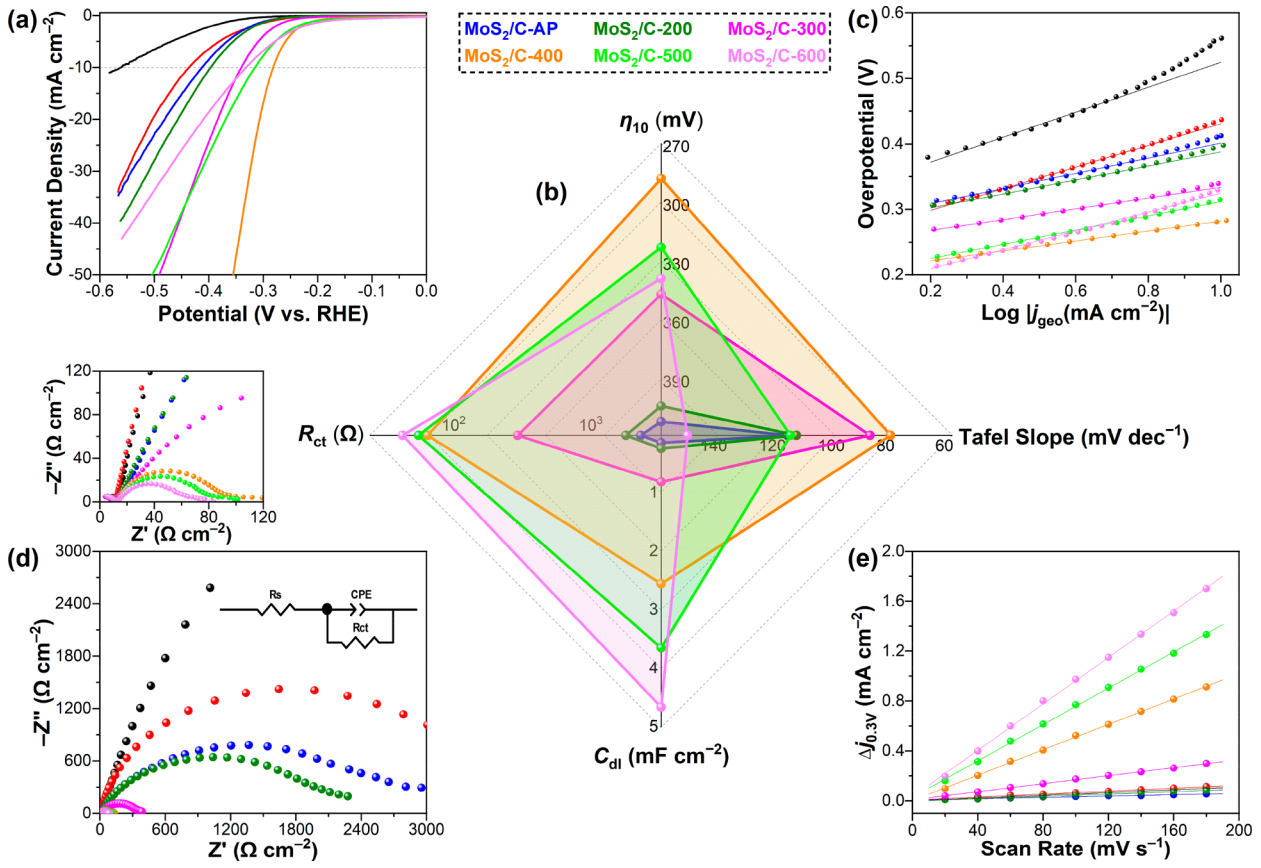

Figure 4. (a) *iR*-compensated LSV polarization curves, (b) a radar chart using η_{10}, Tafel slope, C_{dl}, and R_{ct} as four axes, (c) Tafel plots, (d) Nyquist plots, and (e) differences in current density ($(j_{anodic} - j_{cathodic})/2$) at 0.3 V_{RHE} plotted against the scan rate of calcined MoS_2/C, MoS_2/C-AP, c-MoS_2/C, and Super P. The HER is tested in Ar-saturated 0.5 M H_2SO_4. The inset in (d) is the equivalent circuit model for fitting the impedance spectra. The graph above (d) is an enlargement of the Nyquist plots. All parts of the figure share the same legend based on the line/dot coloring.

to the 2H-MoS_2 basal plane is thermodynamically unfavorable and electron transfer to semiconductive 2H-MoS_2 is slow.[43,44] For the catalysts calcined at temperatures either lower or higher than 400 °C, the Volmer step is also the RDS. In contrast, the Heyrovsky step is the RDS for MoS_2/C-400, manifesting the sluggish electrochemical desorption of H* on the active sites.[45−48] It is thus deduced that the electronic structure of MoS_2 has been modulated by carbon encapsulation to favor the adsorption of H*.

Electrochemical impedance spectroscopy (EIS) measurements are carried out for all the catalysts, and the Nyquist plots are presented in Figure 4d. The solution resistance R_s is determined to be around 10 Ω, which is used for *iR* compensation. The charge transfer resistance R_{ct} represented by the semicircular diameter is compared in the leftward axis of Figure 4b. With an increase in calcination temperature, R_{ct} of the calcined MoS_2/C gradually decreases, indicating a reduced resistance in electron transfer at the electrode/electrolyte interfaces. This agrees with the higher graphitization degree or electrical conductivity of the carbon shell obtained at higher temperatures, as revealed by the Raman analysis in Figure 3d. The double-layer capacitance (C_{dl}) is calculated to assess the electrochemically active surface area. According to the non-Faradaic CV curves (Figure S15), the capacitive current density at 0.3 V_{RHE} is plotted against the scan rate (Figure 4e). After linear fitting, the obtained C_{dl} is compared in the downward axis of Figure 4b. It is found that the C_{dl} value of calcined MoS_2/C increases constantly with the calcination temperature. Given that carbon materials with a high specific surface area also exhibit capacitive behavior, the larger C_{dl} value of MoS_2/C sintered at higher temperatures should be largely due to the carbon shell with a greater thickness. Nonetheless, according to the colored areas linking four key performance indicators in the radar chart of Figure 4b, a better catalyst should cover a larger area and MoS_2/C-400 thus has the best performance among all of the catalysts.

The preceding structural characterizations and catalytic performance hint that the shell thickness of MoS_2/C varies with the calcination temperature. The Rutherford backscattering spectrometry (RBS, Note S2) is then employed for quantification of the carbon shell thickness of calcined unsupported MoS_2, in addition to the depth-profiling XPS. Graphite bulk and thin gold films are utilized to calibrate the energy offset and energy per channel (Figure S16). Figure 5a shows the experimental and simulated RBS spectra using the SIMNRA code.[49] All of the materials present stair-shaped spectra featured by typical bulk samples, indicating their relatively high thicknesses deposited on silicon wafers. The simulated spectra of single-phase MoS_2 and carbon films with different thicknesses and layer configurations are also given in Figure S17. The front edges at channels of 457, 657, 981, 1112, and 1564, representing the elements C, O, Si, S, and Mo, respectively, are indicated. The sharp peak at channel 451 is ascribed to non-Rutherford elastic backscattering. N is not detected due, probably to its low intensity and signal overlapping. Provided that the surface of calcined MoS_2 should

https://doi.org/10.1021/acs.nanolett.2c03181
Nano Lett. 2022, 22, 8763−8770

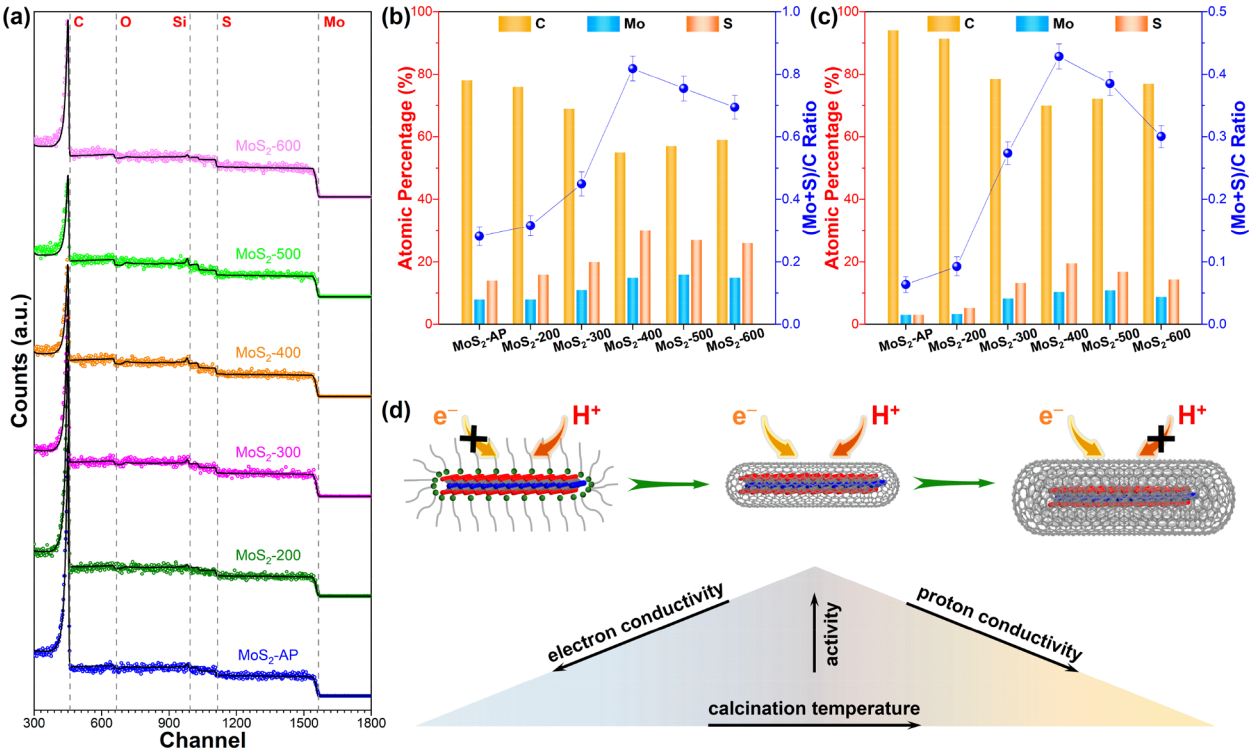

Figure 5. (a) Experimental and simulated RBS spectra and normalized atomic percentages of C, Mo, S, and measured (Mo + S)/C atomic ratios derived from RBS (b) and XPS (c) of the calcined and as-prepared MoS_2. The colored circles and solid lines in (a) refer to the experimental and simulated data, respectively. Channels corresponding to the front edges of C, O, Si, S, and Mo elements are indicated by dashed lines. (d) Schematic illustration of the effect of surface encapsulation on the electron and proton conductivities of identically sized MoS_2 monolayers.

be carbon layers, shifting of the front edges of buried Mo and S elements should be expected due to energy loss of incident ion particles traveling through the carbon layers. However, such shifting is not obvious in Figure 5a, indicating that the carbon layer has a thickness of several nanometers, as revealed by the simulations in Figure S17. The RBS spectra of blank silicon wafer show no major C peak, ruling out the potential origin of adventitious carbon from the solvent or other organic impurities (Figure S18).

Based on the fitted data, the average atomic percentage normalized to C, Mo, and S atoms together with the (Mo + S)/C atomic ratio (Table S1), which quantifies the relative thickness of the carbon shell, is plotted in Figure 5b. MoS_2-AP possesses a high C content that originates from the OAm ligands. Upon calcination, OAm ligands are vaporized, accounting for the ever-decreasing C contents of MoS_2-200, MoS_2-300, and MoS_2-400. At temperatures of 500 and 600 °C, carbonization of OAm ligands becomes the dominant process, leading to higher C contents in comparison to MoS_2-400. The smallest carbon shell thickness is then achieved at 400 °C. Furthermore, the relative thickness is also derived from the XPS data (Table S2). As presented in Figure 5c, the relative thickness derived from XPS follows the exact same variation as the RBS results. In addition to this observation, the Mo/S ratios are in good accord with the stoichiometric ratio of MoS_2.

Given the above, a rational explanation for the volcano-type HER activity trend can be made, which is briefly illustrated in Figure 5d. First, TEM and XRD results show that the lateral size and monolayer structure of calcined MoS_2 are well preserved, excluding the MoS_2 size effect on HER activity. As collectively revealed by multiple techniques, MoS_2/C-AP and MoS_2/C-200 are strongly capped by OAm, deactivating the surface-active sites for the HER. A Tafel analysis indicates that the Volmer step that involves proton-coupled electron transfer is rate-determining for these catalysts. Considering the large R_{ct} from EIS measurements, we believe that the low electron conductivity should be held accountable for the poor activity of these OAm-ligated catalysts. Removal and translation of OAm by calcination gradually release the active sites and thus result in the enhanced HER activity of MoS_2/C-300 and MoS_2/C-400. In addition, the carbon shell tunes the electronic structure of the catalyst that eventually favors the adsorption of H*, changing the RDS to the Heyrovsky step. Further elevation of the calcination temperature leads to an intensified carbonization of OAm, and MoS_2 monolayers are thus coated by thicker shells. The RDS for both MoS_2/C-500 and MoS_2/C-600 is then shifted back to the Volmer step. By virtue of the improved graphitization degree and reduced R_{ct} from EIS results, their degenerative kinetics should be attributed to the inadequate proton conductivity rather than the electron conductivity as above.

To summarize, we have investigated the effects of thermal calcination on the ligand carbonization and carbon shell thickness on the catalytic properties of MoS_2 by utilizing OAm-ligated MoS_2 monolayers. OAm is found to be gradually pyrolyzed into a carbon shell as the calcination temperature increases. When tested toward an acidic HER, the calcined catalysts deliver a volcano-type activity trend with MoS_2/C-400 presenting the highest activity. RBS and depth-profiling XPS results indicate that the best-performing MoS_2/C-400 is neither capped by excessive OAm ligands nor covered by thick carbon layers, in sharp contrast to other catalysts calcined at higher or lower temperatures. In this case, the proton and electron transfer are both improved to surmount the slow kinetics of the Volmer step. This study not only gives attention to the judicious

https://doi.org/10.1021/acs.nanolett.2c03181
Nano Lett. 2022, 22, 8763−8770

selection of calcination conditions for ligand removal but also unambiguously uncovers the shell thickness effect of core−shell structured catalysts on the catalytic activity.

■ ASSOCIATED CONTENT

Supporting Information

The Supporting Information is available free of charge at https://pubs.acs.org/doi/10.1021/acs.nanolett.2c03181.

Experimental section, briefs of Tafel analysis and RBS, normalized elemental contents, and additional XRD, ATR-FTIR, SEM, XPS, CV, and RBS data (PDF)

■ AUTHOR INFORMATION

Corresponding Authors

Xing Lu − *State Key Laboratory of Materials Processing and Die & Mould Technology, School of Materials Science and Engineering, Huazhong University of Science and Technology, Wuhan 430074, People's Republic of China;* orcid.org/0000-0003-2741-8733; Email: lux@hust.edu.cn

Zhixin Yu − *Institute of New Energy, School of Chemistry and Chemical Engineering, Shaoxing University, Shaoxing 312000, People's Republic of China; Department of Energy and Petroleum Engineering, University of Stavanger, 4036 Stavanger, Norway;* orcid.org/0000-0003-2446-6537; Email: zhixin.yu@uis.no

Authors

Kun Guo − *State Key Laboratory of Materials Processing and Die & Mould Technology, School of Materials Science and Engineering, Huazhong University of Science and Technology, Wuhan 430074, People's Republic of China; Department of Chemistry, The University of Manchester, Manchester M13 9PL, United Kingdom;* orcid.org/0000-0002-4822-5984

Litao Chang − *Shanghai Institute of Applied Physics, Chinese Academy of Sciences, Shanghai 201800, People's Republic of China*

Ning Li − *State Key Laboratory of Materials Processing and Die & Mould Technology, School of Materials Science and Engineering, Huazhong University of Science and Technology, Wuhan 430074, People's Republic of China*

Lipiao Bao − *State Key Laboratory of Materials Processing and Die & Mould Technology, School of Materials Science and Engineering, Huazhong University of Science and Technology, Wuhan 430074, People's Republic of China*

Samir de Moraes Shubeita − *Dalton Cumbrian Facility, The University of Manchester, Cumbria CA24 3HA, United Kingdom*

Aliaksandr Baidak − *Department of Chemistry, The University of Manchester, Manchester M13 9PL, United Kingdom; Dalton Cumbrian Facility, The University of Manchester, Cumbria CA24 3HA, United Kingdom;* orcid.org/0000-0001-7064-2082

Complete contact information is available at: https://pubs.acs.org/10.1021/acs.nanolett.2c03181

Notes

The authors declare no competing financial interest.

■ ACKNOWLEDGMENTS

This work was supported by the National Natural Science Foundation of China (21925104), the Natural Science Foundation of Hubei Province (2021CFA020), the Engineering and Physical Sciences Research Council, UK (EP/R042179/1), and the start-up funding of Huazhong University of Science and Technology (3004110178) and Shaoxing University (13011001015001/6085). The authors also acknowledge the support of The University of Manchester's Dalton Cumbrian Facility (DCF), a partner in the National Nuclear User Facility, the EPSRC UK National Ion Beam Centre, and the Henry Royce Institute, and the support of the Analytical and Testing Center, Huazhong University of Science and Technology.

■ REFERENCES

(1) Lee, K. J.; McCarthy, B. D.; Dempsey, J. L. On Decomposition, Degradation, and Voltammetric Deviation: The Electrochemist's Field Guide to Identifying Precatalyst Transformation. *Chem. Soc. Rev.* **2019**, *48*, 2927−2945.

(2) Jiang, H.; He, Q.; Zhang, Y.; Song, L. Structural Self-Reconstruction of Catalysts in Electrocatalysis. *Acc. Chem. Res.* **2018**, *51*, 2968−2977.

(3) Wang, J.; Kim, S.-J.; Liu, J.; Gao, Y.; Choi, S.; Han, J.; Shin, H.; Jo, S.; Kim, J.; Ciucci, F.; Kim, H.; Li, Q.; Yang, W.; Long, X.; Yang, S.; Cho, S.-P.; Chae, K. H.; Kim, M. G.; Kim, H.; Lim, J. Redirecting Dynamic Surface Restructuring of a Layered Transition Metal Oxide Catalyst for Superior Water Oxidation. *Nat. Catal.* **2021**, *4*, 212−222.

(4) Wang, J.; Tan, H. Y.; Kuo, T. R.; Lin, S. C.; Hsu, C. S.; Zhu, Y.; Chu, Y. C.; Chen, T. L.; Lee, J. F.; Chen, H. M. In Situ Identifying the Dynamic Structure Behind Activity of Atomically Dispersed Platinum Catalyst toward Hydrogen Evolution Reaction. *Small* **2021**, *17*, 2005713.

(5) Lu, X.; Wu, Y.; Yuan, X.; Wang, H. An Integrated CO_2 Electrolyzer and Formate Fuel Cell Enabled by a Reversibly Restructuring Pb−Pd Bimetallic Catalyst. *Angew. Chem., Int. Ed.* **2019**, *58*, 4031−4035.

(6) Yan, B.; Krishnamurthy, D.; Hendon, C. H.; Deshpande, S.; Surendranath, Y.; Viswanathan, V. Surface Restructuring of Nickel Sulfide Generates Optimally Coordinated Active Sites for Oxygen Reduction Catalysis. *Joule* **2017**, *1*, 600−612.

(7) Gao, C.; Lyu, F.; Yin, Y. Encapsulated Metal Nanoparticles for Catalysis. *Chem. Rev.* **2021**, *121*, 834−881.

(8) Deng, J.; Deng, D.; Bao, X. Robust Catalysis on 2D Materials Encapsulating Metals: Concept, Application, and Perspective. *Adv. Mater.* **2017**, *29*, 1606967.

(9) Gawande, M. B.; Goswami, A.; Asefa, T.; Guo, H.; Biradar, A. V.; Peng, D. L.; Zboril, R.; Varma, R. S. Core−Shell Nanoparticles: Synthesis and Applications in Catalysis and Electrocatalysis. *Chem. Soc. Rev.* **2015**, *44*, 7540−7590.

(10) Nocera, D. G. Proton-Coupled Electron Transfer: The Engine of Energy Conversion and Storage. *J. Am. Chem. Soc.* **2022**, *144*, 1069−1081.

(11) Koper, M. T. M. Theory of Multiple Proton−Electron Transfer Reactions and Its Implications for Electrocatalysis. *Chem. Sci.* **2013**, *4*, 2710−2723.

(12) Hu, S.; Lozada-Hidalgo, M.; Wang, F. C.; Mishchenko, A.; Schedin, F.; Nair, R. R.; Hill, E. W.; Boukhvalov, D. W.; Katsnelson, M. I.; Dryfe, R. A.; Grigorieva, I. V.; Wu, H. A.; Geim, A. K. Proton Transport through One-Atom-Thick Crystals. *Nature* **2014**, *516*, 227−230.

(13) Lozada-Hidalgo, M.; Hu, S.; Marshall, O.; Mishchenko, A.; Grigorenko, A. N.; Dryfe, R. A.; Radha, B.; Grigorieva, I. V.; Geim, A. K. Sieving Hydrogen Isotopes through Two-Dimensional Crystals. *Science* **2016**, *351*, 68−70.

(14) Sun, P. Z.; Yang, Q.; Kuang, W. J.; Stebunov, Y. V.; Xiong, W. Q.; Yu, J.; Nair, R. R.; Katsnelson, M. I.; Yuan, S. J.; Grigorieva, I. V.; Lozada-Hidalgo, M.; Wang, F. C.; Geim, A. K. Limits on Gas Impermeability of Graphene. *Nature* **2020**, *579*, 229−232.

(15) Hu, K.; Ohto, T.; Nagata, Y.; Wakisaka, M.; Aoki, Y.; Fujita, J. I.; Ito, Y. Catalytic Activity of Graphene-Covered Non-Noble Metals Governed by Proton Penetration in Electrochemical Hydrogen Evolution Reaction. *Nat. Commun.* **2021**, *12*, 203.

(16) Shih, A. J.; Arulmozhi, N.; Koper, M. T. M. Electrocatalysis under Cover: Enhanced Hydrogen Evolution via Defective Graphene-Covered Pt(111). *ACS Catal.* **2021**, *11*, 10892−10901.
(17) Deng, J.; Ren, P.; Deng, D.; Bao, X. Enhanced Electron Penetration through an Ultrathin Graphene Layer for Highly Efficient Catalysis of the Hydrogen Evolution Reaction. *Angew. Chem., Int. Ed.* **2015**, *54*, 2100−2104.
(18) Wang, H. F.; Chen, L.; Pang, H.; Kaskel, S.; Xu, Q. MOF-Derived Electrocatalysts for Oxygen Reduction, Oxygen Evolution and Hydrogen Evolution Reactions. *Chem. Soc. Rev.* **2020**, *49*, 1414−1448.
(19) Wang, T.; Cao, X.; Jiao, L. MOFs-Derived Carbon-Based Metal Catalysts for Energy-Related Electrocatalysis. *Small* **2021**, *17*, 2004398.
(20) Liang, Z.; Qiu, T.; Gao, S.; Zhong, R.; Zou, R. Multi-Scale Design of Metal−Organic Framework-Derived Materials for Energy Electrocatalysis. *Adv. Energy Mater.* **2022**, *12*, 2003410.
(21) Huang, Y.; Chen, Y. C.; Xu, M. J.; Asset, T.; Tieu, P.; Gili, A.; Kulkarni, D.; De Andrade, V.; De Carlo, F.; Barnard, H. S.; Doran, A.; Parkinson, D. Y.; Pan, X. Q.; Atanassov, P.; Zenyuk, I. V. Catalysts by Pyrolysis: Direct Observation of Chemical and Morphological Transformations Leading to Transition Metal-Nitrogen-Carbon Materials. *Mater. Today* **2021**, *47*, 53−68.
(22) Chen, M. X.; Zhu, M.; Zuo, M.; Chu, S. Q.; Zhang, J.; Wu, Y.; Liang, H. W.; Feng, X. Identification of Catalytic Sites for Oxygen Reduction in Metal/Nitrogen-Doped Carbons with Encapsulated Metal Nanoparticles. *Angew. Chem., Int. Ed.* **2020**, *59*, 1627−1633.
(23) Jiang, W. J.; Gu, L.; Li, L.; Zhang, Y.; Zhang, X.; Zhang, L. J.; Wang, J. Q.; Hu, J. S.; Wei, Z.; Wan, L. J. Understanding the High Activity of Fe−N−C Electrocatalysts in Oxygen Reduction: Fe/Fe_3C Nanoparticles Boost the Activity of $Fe-N_x$. *J. Am. Chem. Soc.* **2016**, *138*, 3570−3578.
(24) Wu, L.; Mendoza-Garcia, A.; Li, Q.; Sun, S. Organic Phase Syntheses of Magnetic Nanoparticles and Their Applications. *Chem. Rev.* **2016**, *116*, 10473−10512.
(25) Nasilowski, M.; Mahler, B.; Lhuillier, E.; Ithurria, S.; Dubertret, B. Two-Dimensional Colloidal Nanocrystals. *Chem. Rev.* **2016**, *116*, 10934−10982.
(26) van Embden, J.; Chesman, A. S. R.; Jasieniak, J. J. The Heat-up Synthesis of Colloidal Nanocrystals. *Chem. Mater.* **2015**, *27*, 2246−2285.
(27) Mohapatra, P.; Shaw, S.; Mendivelso-Perez, D.; Bobbitt, J. M.; Silva, T. F.; Naab, F.; Yuan, B.; Tian, X.; Smith, E. A.; Cademartiri, L. Calcination Does Not Remove All Carbon from Colloidal Nanocrystal Assemblies. *Nat. Commun.* **2017**, *8*, 2038.
(28) Xiao, F.; Qin, X.; Xu, M.; Zhu, S.; Zhang, L.; Hong, Y.; Choi, S.-I.; Chang, Q.; Xu, Y.; Pan, X.; Shao, M. Impact of Heat Treatment on the Electrochemical Properties of Carbon-Supported Octahedral Pt−Ni Nanoparticles. *ACS Catal.* **2019**, *9*, 11189−11198.
(29) Zhang, L.; Liu, H.; Liu, S.; Norouzi Banis, M.; Song, Z.; Li, J.; Yang, L.; Markiewicz, M.; Zhao, Y.; Li, R.; Zheng, M.; Ye, S.; Zhao, Z.-J.; Botton, G. A.; Sun, X. Pt/Pd Single-Atom Alloys as Highly Active Electrochemical Catalysts and the Origin of Enhanced Activity. *ACS Catal.* **2019**, *9*, 9350−9358.
(30) Li, Z.; Wang, Z.; Kawi, S. Sintering and Coke Resistant Core/Yolk Shell Catalyst for Hydrocarbon Reforming. *ChemCatChem.* **2019**, *11*, 202−224.
(31) Cargnello, M. Colloidal Nanocrystals as Building Blocks for Well-Defined Heterogeneous Catalysts. *Chem. Mater.* **2019**, *31*, 576−596.
(32) Guo, K.; Ding, Y.; Yu, Z. One-Step Synthesis of Ultrafine MoNiS and MoCoS Monolayers as High-Performance Catalysts for Hydrodesulfurization and Hydrodenitrogenation. *Appl. Catal. B: Environ.* **2018**, *239*, 433−440.
(33) Mourdikoudis, S.; Liz-Marzan, L. M. Oleylamine in Nanoparticle Synthesis. *Chem. Mater.* **2013**, *25*, 1465−1476.
(34) Yu, Y.; Yang, W.; Sun, X.; Zhu, W.; Li, X. Z.; Sellmyer, D. J.; Sun, S. Monodisperse MPt (M = Fe, Co, Ni, Cu, Zn) Nanoparticles Prepared from a Facile Oleylamine Reduction of Metal Salts. *Nano Lett.* **2014**, *14*, 2778−2782.
(35) Savjani, N.; Lewis, E. A.; Bissett, M. A.; Brent, J. R.; Dryfe, R. A. W.; Haigh, S. J.; O'Brien, P. Synthesis of Lateral Size-Controlled Monolayer 1*H*-MoS_2@Oleylamine as Supercapacitor Electrodes. *Chem. Mater.* **2016**, *28*, 657−664.
(36) Xu, Z. C.; Shen, C. M.; Hou, Y. L.; Gao, H. J.; Sun, S. S. Oleylamine as Both Reducing Agent and Stabilizer in a Facile Synthesis of Magnetite Nanoparticles. *Chem. Mater.* **2009**, *21*, 1778−1780.
(37) Wilson, D.; Langell, M. A. XPS Analysis of Oleylamine/Oleic Acid Capped Fe_3O_4 Nanoparticles as a Function of Temperature. *Appl. Surf. Sci.* **2014**, *303*, 6−13.
(38) Ganatra, R.; Zhang, Q. Few-Layer MoS_2: A Promising Layered Semiconductor. *ACS Nano* **2014**, *8*, 4074−4099.
(39) Najmaei, S.; Liu, Z.; Ajayan, P. M.; Lou, J. Thermal Effects on the Characteristic Raman Spectrum of Molybdenum Disulfide (MoS_2) of Varying Thicknesses. *Appl. Phys. Lett.* **2012**, *100*, 013106.
(40) Kibsgaard, J.; Chen, Z.; Reinecke, B. N.; Jaramillo, T. F. Engineering the Surface Structure of MoS_2 to Preferentially Expose Active Edge Sites for Electrocatalysis. *Nat. Mater.* **2012**, *11*, 963−969.
(41) Li, H.; Tsai, C.; Koh, A. L.; Cai, L.; Contryman, A. W.; Fragapane, A. H.; Zhao, J.; Han, H. S.; Manoharan, H. C.; Abild-Pedersen, F.; Norskov, J. K.; Zheng, X. Activating and Optimizing MoS_2 Basal Planes for Hydrogen Evolution through the Formation of Strained Sulphur Vacancies. *Nat. Mater.* **2016**, *15*, 48−53.
(42) Zhou, M.; Zhang, Z.; Huang, K.; Shi, Z.; Xie, R.; Yang, W. Colloidal Preparation and Electrocatalytic Hydrogen Production of MoS_2 and WS_2 Nanosheets with Controllable Lateral Sizes and Layer Numbers. *Nanoscale* **2016**, *8*, 15262−15272.
(43) Peto, J.; Ollar, T.; Vancso, P.; Popov, Z. I.; Magda, G. Z.; Dobrik, G.; Hwang, C.; Sorokin, P. B.; Tapaszto, L. Spontaneous Doping of the Basal Plane of MoS_2 Single Layers through Oxygen Substitution under Ambient Conditions. *Nat. Chem.* **2018**, *10*, 1246−1251.
(44) Voiry, D.; Fullon, R.; Yang, J.; de Carvalho Castro, E. S. C.; Kappera, R.; Bozkurt, I.; Kaplan, D.; Lagos, M. J.; Batson, P. E.; Gupta, G.; Mohite, A. D.; Dong, L.; Er, D.; Shenoy, V. B.; Asefa, T.; Chhowalla, M. The Role of Electronic Coupling between Substrate and 2D MoS_2 Nanosheets in Electrocatalytic Production of Hydrogen. *Nat. Mater.* **2016**, *15*, 1003−1009.
(45) Shen, S.; Lin, Z.; Song, K.; Wang, Z.; Huang, L.; Yan, L.; Meng, F.; Zhang, Q.; Gu, L.; Zhong, W. Reversed Active Sites Boost the Intrinsic Activity of Graphene-Like Cobalt Selenide for Hydrogen Evolution. *Angew. Chem., Int. Ed.* **2021**, *60*, 12360−12365.
(46) Sun, Y.; Li, X.; Zhang, T.; Xu, K.; Yang, Y.; Chen, G.; Li, C.; Xie, Y. Nitrogen-Doped Cobalt Diselenide with Cubic Phase Maintained for Enhanced Alkaline Hydrogen Evolution. *Angew. Chem., Int. Ed.* **2021**, *60*, 21575−21582.
(47) Miao, R.; Dutta, B.; Sahoo, S.; He, J.; Zhong, W.; Cetegen, S. A.; Jiang, T.; Alpay, S. P.; Suib, S. L. Mesoporous Iron Sulfide for Highly Efficient Electrocatalytic Hydrogen Evolution. *J. Am. Chem. Soc.* **2017**, *139*, 13604−13607.
(48) Zhou, W.; Xiong, T.; Shi, C.; Zhou, J.; Zhou, K.; Zhu, N.; Li, L.; Tang, Z.; Chen, S. Bioreduction of Precious Metals by Microorganism: Efficient Gold@N-Doped Carbon Electrocatalysts for the Hydrogen Evolution Reaction. *Angew. Chem., Int. Ed.* **2016**, *55*, 8416−8420.
(49) Mayer, M. SIMNRA, a Simulation Program for the Analysis of NRA, RBS and ERDA. *AIP Conf. Proc.* **1999**, *475*, 541−544.

https://doi.org/10.1021/acs.nanolett.2c03181
Nano Lett. 2022, 22, 8763−8770